Utrecht University

SuperSILs: improving resolution and targeting accuracy of fluorescence microscopy for cryo-CLEM

by

Koen Jurgens

Layman’s summary

Proteins are large molecules responsible for many functions within organisms. The investigation of their structures is crucial to understand how their mechanisms work. To locate particular proteins in a cell as accurately as possible, a light microscope must have achieve high resolutions. Resolution is defined as the ability to distinguish two objects from each other. The better the quality of the lenses in a light microscope, the higher the resolution. If any lens is of lower quality, the objects are displayed less representatively. We have studied a lens of high-quality named “superSIL”, which can be used to increase the resolution of any microscope. The lens of the superSIL is made from a special material that can collect and focus light better than the lenses in a light microscope. In theory, it can be added to any light microscope set-up. Thus, we investigated the abilities of the superSIL by evaluating the performance of our light microscope before and after inclusion of the superSIL, and by comparing the results afterwards. It turned out that the resolution substantially improved in 2D, so our with the light microscope recorded objects were represented more correctly. However, varying results were observed in the third dimension. Some experiments were carried out at temperatures around -170 to -180°C, so ice was probably formed after a while. Light behaves differently in ice than in air, causing blurring of our objects during their recording. To conclude, the superSIL can achieve higher resolutions to make light microscopy more appealing for usage in locating proteins. Next, their structures could be investigated with other techniques.

Lekensamenvatting

Eiwitten zijn grote moleculen die verantwoordelijk zijn voor vele functies in organismen. Het onderzoek van hun structuren is cruciaal om te begrijpen hoe hun mechanismen werken. Om bepaalde eiwitten in een cel zo nauwkeurig mogelijk te lokaliseren moet een lichtmicroscoop hoge resoluties verschaffen. Resolutie wordt gedefinieerd als het vermogen om twee objecten van elkaar te onderscheiden. Hoe beter de kwaliteit van de lenzen in een lichtmicroscoop, hoe hoger de resolutie. Als een lens van lagere kwaliteit is, worden de objecten minder representatief weergegeven. We hebben een lens van hoge kwaliteit bestudeerd, "superSIL" genaamd, die gebruikt kan worden om de resolutie van een microscoop te verhogen. De lens van de superSIL is gemaakt van een speciaal materiaal dat licht beter kan opvangen en focussen dan de lenzen van een lichtmicroscoop. In theorie kan het aan elke lichtmicroscoopopstelling worden toegevoegd. Daarom hebben we de capaciteiten van de superSIL onderzocht door de prestaties van onze lichtmicroscoop voor en na toevoeging van de superSIL te evalueren en door de resultaten daarna te vergelijken. Het bleek dat de resolutie in 2D aanzienlijk verbeterde, waardoor onze met de lichtmicroscoop opgenomen objecten correcter werden weergegeven. In de derde dimensie werden echter wisselende resultaten waargenomen. Sommige experimenten zijn uitgevoerd bij temperaturen van -170 à -180°C, dus waarschijnlijk is er na een tijdje ijs gevormd. Licht gedraagt zich in ijs anders dan in lucht, waardoor objecten vervaagd werden tijdens het opnemen. De conclusie is dat de superSIL hogere resoluties kan verschaffen om lichtmicroscopie aantrekkelijker te maken voor het gebruik van lokaliseren van eiwitten. Vervolgens zouden hun structuren met andere technieken kunnen worden onderzocht.

Archaea is het derde domein naast bacteriën en eukaryoten (eukaryoten zijn organismen waarvan de cellen een celkern bezitten), en bevat veel soorten met unieke kenmerken, waaronder hun vermogen om te overleven in extreme milieus. Eén soort genaamd *Pyrococcus furiosus* leeft optimaal bij temperaturen rond de 100°C. Normaal gesproken verliezen veel eiwitten bij deze temperaturen hun structuur en bijbehorende functies. Daarom is het interessant om uit te zoeken hoe *Pyrococcus furiosus* zich verdedigt tegen zijn omgeving. Tijdens onze zoektocht naar bepaalde deeltjes om de structuur ervan op te helderen, kwamen we buisvormige structuren tegen die deze deeltjes omsloten. De buis blijkt samengesteld te zijn uit kleine eiwitten die erg op elkaar lijken, en elke ring in de buis bevatte 17 van deze eiwitten. De identiteit van dit eiwit is echter nog onbekend, maar zou uiteindelijk inzicht kunnen geven in de moleculaire interactie tussen de buizen en de deeltjes die in de buizen zitten. Bovendien kunnen de buizen deel uitmaken van de strategie die *Pyrococcus furiosus* gebruikt om de inhoud in zijn cellen te beschermen. Voor zover wij weten, is er nu voor het eerst een model voor deze buisvormige structuren voorgesteld.

Table of contents

SuperSILs: improving resolution and targeting accuracy of fluorescence microscopy for cryo-CLEM

Koen Jurgens

Structural Biochemistry, Bijvoet Centre for Biomolecular Research, Utrecht University, Universiteitsweg 99, 3584 CG Utrecht, The Netherlands.

Cryo-electron microscopy (cryo-EM) is a powerful tool to study protein structures at high resolution, crucial in advancing our understanding of their mode of action and biological functioning. The main disadvantage of cryo-EM is its limited field of view, making the task to locate and target the region of interest (ROI) cumbersome. A solution lies within cryo-fluorescence light microscopy (cryo-FLM), because large volumes can be examined, and both techniques can be combined into correlative light and electron microscopy (CLEM). However, the lack of compatible high numerical aperture (NA) objective lenses under cryogenic temperatures in FLM causes a resolution gap between EM and FLM. Here, super-hemispherical solid immersion lenses (superSILs), an easy to implement solution for most microscope set-ups and compatible with cryo-conditions, were used to determine the improvement in instrument performance. Primarily the lateral resolution improved substantially, approaching the true value of the recorded objects. Improving the image correlation accuracy will make cryo-CLEM more straightforward, and its popularity could grow among techniques that resolve structures.

Introduction

Cellular processes are crucial for the functioning of cells, tissues and complete organs. These rely on protein-protein interactions and involve many complex biomolecular machineries. Structural biology aims to visualize biomacromolecules in 3D and at atomic resolution to obtain insight into their mode of action. One effective technique to study structures and dynamics, even if the assemblies are flexible, is cryo-electron microscopy (cryo-EM). Cryo-EM became even more powerful after the introduction of better detectors with fast readout and improved sensitivity, a development known as the 'resolution revolution' (Kühlbrandt, 2014). However, achieving high resolution with cryo-EM results in a limited field of view making it difficult to find the location of the region of interest (ROI). This challenge can be solved with cryo-fluorescence light microscopy (cryo-FLM), because it allows for working with large volumes containing many cells or for targeting specific subcellular locations. To benefit research maximally in terms of field of view, resolution and context analysis, both techniques can be combined using a correlative light and electron microscopy (CLEM) approach. However, a large obstacle in this workflow is the resolution gap between cryo-EM and cryo-FLM, resulting in less precise localization and targeting of the ROI.

Cryo-electron tomography (cryo-ET) is a subdomain of cryo-EM to examine ROIs and provides a macromolecular view of the crowded environment inside cells by recording 2D images while tilting samples and reconstructing them accordingly (Asano *et al.*, 2016; Schur, 2019). Each cell is examined individually and the field of view is only a very small fraction of the studied cell, drastically reducing the throughput and creating the risk of biased sampling (Sartori *et al.*, 2007). This is due to the high magnification and because the samples must be thin (<200 nm) for tomography. Cells are often thinned with focused ion beam (FIB) milling, because it allows for precise targeting to the ROI at nanometer resolution while minimizing any damage to the sample (Marko *et al.*, 2007; Rigort *et al.*, 2012). To identify ROIs more accurately, FLM can be used, because fluorescence can be made specific to a particular protein or event.

In FLM, fluorophores within the sample emit light upon excitation. The emission filter that lets light emitted by the fluorophores through and blocks other wavelengths, creates the contrast between fluorescent and non-fluorescent objects after photons are gathered by the objective lens. The numerical aperture (NA) of an objective lens describes how much light is captured:

$$NA = n \sin \theta \qquad (1)$$

where NA is the numerical aperture of an objective lens, n is the refractive index (RI) of the medium between the sample and the objective, and θ is the maximal half-angle of the light cone that can enter or exit the lens. The resolution of the final image is dependent on the NA of the objective lens, assuming the wavelength does not alter:

$$R = \frac{0.61\,\lambda}{NA} \qquad (2)$$

where R is the resolution, and λ is the illumination wavelength. Objective lenses with NAs >1 (and preferably ≥1.4) are required to achieve high resolution, but these generally need immersion fluids to couple the sample to the objective (Faoro *et al.*, 2018). Although the NA mainly defines the maximal achievable resolution of a light microscope, the type of imaging technique is also a contributing factor. Widefield microscopy is the conventional method, whereby the entire sample is illuminated including out-of-focus regions, which causes blurring in the final image. Spinning disc confocal microscopy (SDCM) possesses the ability to avoid out-of-focus regions and thus specifically image the ROI. As a consequence, the depth of field can be controlled, the background signal away from the focal plane can be reduced or even eliminated, and serial optical sections from thick specimens can be collected (Elliott, 2020). Moreover, the lateral and axial resolutions are better when compared to widefield (Cox *et al.*, 1982; Paddock & Eliceiri, 2014). Thus, SDCM has multiple advantages over widefield microscopy.

Besides, cryogenic conditions increase the sensitivity of FLM measurements, as the number of photons emitted by fluorophores within the sample before bleaching increases substantially. However, cryogenic conditions also come with complications, because high resolution cryo-FLM is limited by mainly two factors. Namely, a lack of objective lenses that can be cooled to cryogenic temperatures (Schellenberger *et al.*, 2014), and the fact that liquid media freeze under these conditions. Cryo-immersion lenses offering NA values >1 are not available, so dry objectives (NA ≤0.9) operating at a long working distance are mostly used. This results in less light being collected by the lenses, and ultimately in a lower resolution cryo-FLM (Wang *et al.*, 2019). The already challenging correlation with cryo-ET data becomes more complicated because the resolution gap is already the major restriction for successful cryo-CLEM. The resolution gap needs to be narrowed by enacting high resolution cryo-FLM for reliable cryo-CLEM across a range of biological applications. If these challenges could be overcome, the use of cryo-fixation could become more routine in FLM, with the added benefit that rapid freezing is more effective than chemical fixation at preserving ultrastructure and minimizing artefacts (Gilkey & Staehelin, 1986).

One way to address this NA limitation for cryo-FLM is to image samples mounted on super-hemispherical solid immersion lenses (superSILs) that help collect the fluorescent signal. SuperSILs consist of a solid material of high RI, increasing the effective NA of the objective lens, and hence increasing the spatial resolution of the objective lens (Wang *et al.*, 2019). In addition, the superSIL also entails an extra high magnification. Although the superSILs seem promising, reported applications in the literature are limited. One group demonstrated that the superSIL substantially increases the resolution not only for traditional FLM, but also for the super-resolution technique stochastic optical reconstruction microscopy (STORM) (Rust *et al.*, 2006; Wang *et al.*, 2019). The superSIL images they obtained where magnified by almost five times. Therefore, we wanted to know if the superSILs could be applicable to our cryo-CLEM workflow. Specifically, we wanted to test if their performance is preserved in our hands, because the possibility exists that the usage in practice does not match the theoretical capabilities of the superSIL. However, the main goal was to enhance the resolution and precision of our light microscope by using the superSIL.

The current microscope set-up was first evaluated quantitatively by measuring the point spread function (PSF) and drift to ensure a trustworthy baseline for performance comparisons. For this purpose, fluorescent beads were used as a calibration standard. This evaluation was repeated after implementation of the superSILs to characterize the improvements, both at room temperature (RT) and under cryo-conditions. With the addition of the superSIL, the PSF of the fluorescent calibration beads was closer to its true value in the lateral dimensions, meaning a lateral resolution improvement of our instrument. Additionally, the superSIL operated better under cryo-conditions, improving axial resolution when compared with room temperature measurements.

Results

Performance evaluation of the current microscope set-up under various circumstances

The first round of PSF data acquisition was performed in widefield mode to establish a baseline and to optimize several parameters such as the bead concentration and the distance between images in the axial direction by visual assessment. Then, the PSF was determined with SDCM for better lateral and axial

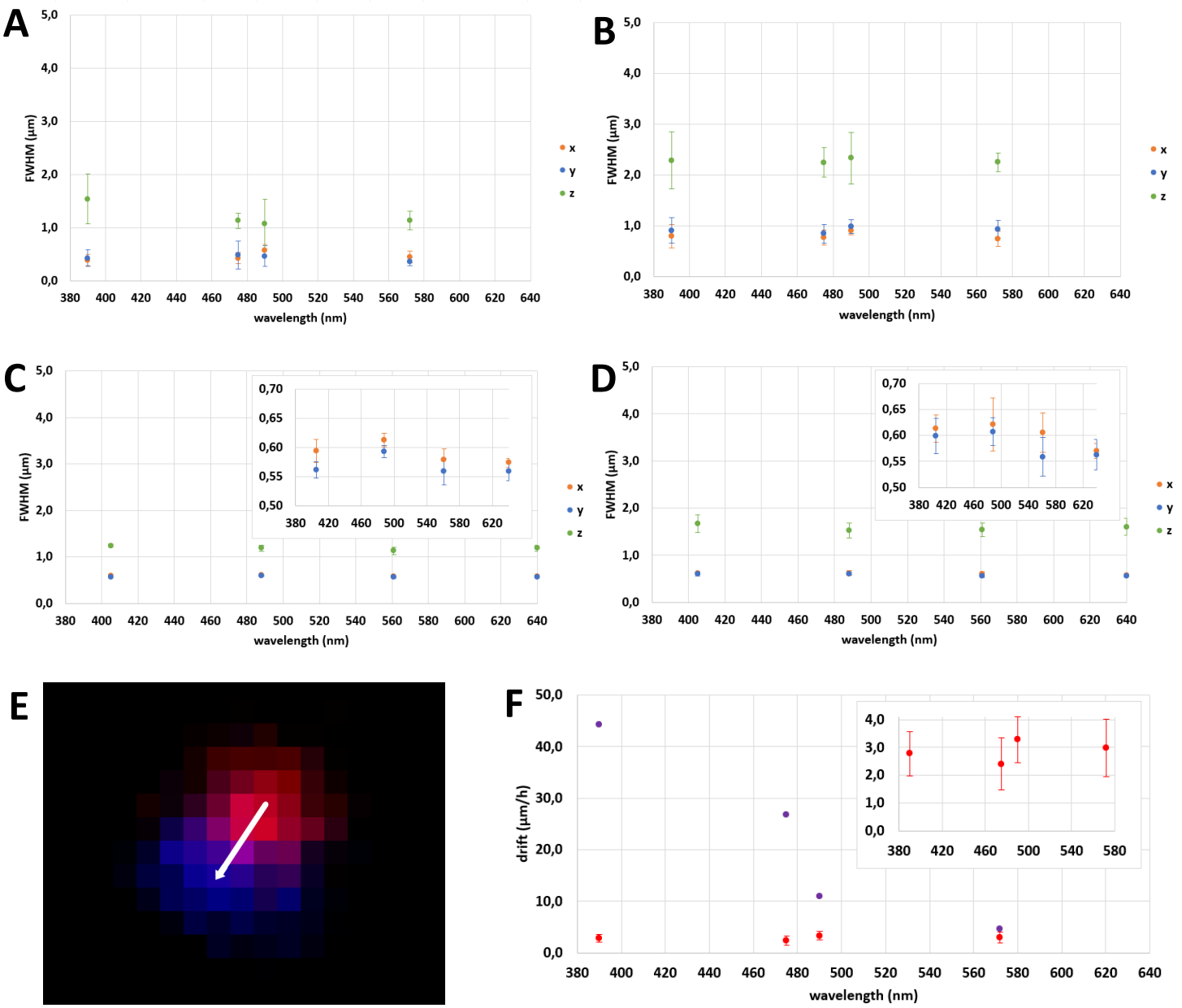

Fig. 1 Instrument performance evaluation without superSIL. PSF profiles in x (orange), y (blue) and z (green) directions. Tetraspeck beads were imaged with widefield at RT (**A**) or under cryogenic conditions (**B**), and with SDCM at RT (**C**) or under cryo-conditions (**D**). Size of beads was 0.5 µm, except for **A**, where 0.1 µm beads were used. Measured PSFs were averaged per dimension per wavelength, error bars show the fluctuations across PSFs (n=8). In **C+D**, the insets show the x and y dimensions at a different scale for clarity. **E.** The start (red) and end (blue) positions of one bead and a white arrow drawn to show the direction of the drift. **F.** Average drift rates, recorded with widefield over 10 min. at RT (red) and under cryogenic conditions (purple), error bars show the fluctuations across time lapses (n=3). The inset shows the RT values at a different scale for clarity.

resolution, which in theory accompanies with a reduction in the full width at half maximum (FWHM) height of the PSF. Multiple diameters (0.1 µm, 0.5 µm and 1.0 µm) of fluorescent Tetraspeck beads were available for imaging the PSF. For more precise measurements, we aimed to use the smallest beads However, their signal was undetectable when imaged under cryo-conditions with widefield and for all SDCM imaging unfortunately. For increased signal, and with the known risk of overestimating the PSF, 0.5 µm beads were used instead. For each imaging modality, the instrument features four wavelengths spread over the visible light spectrum for fluorescence imaging (see Materials & Methods for details), so all four were used to examine if any PSF dissimilarities appeared for the different wavelengths. After image recording, the MetroloJ plugin (Matthews & Cordelières, 2010) for ImageJ (Rueden *et al.*, 2017) was used to generate PSF profiles for single beads (Fig. 1A-D). With widefield at RT, measured values were mostly around 0.4 – 0.5 µm in lateral dimensions and around 1.0 – 1.5 µm in the axial dimension. Although comparison data for the widefield measurements at RT are absent, it demonstrates the best possible performance of our

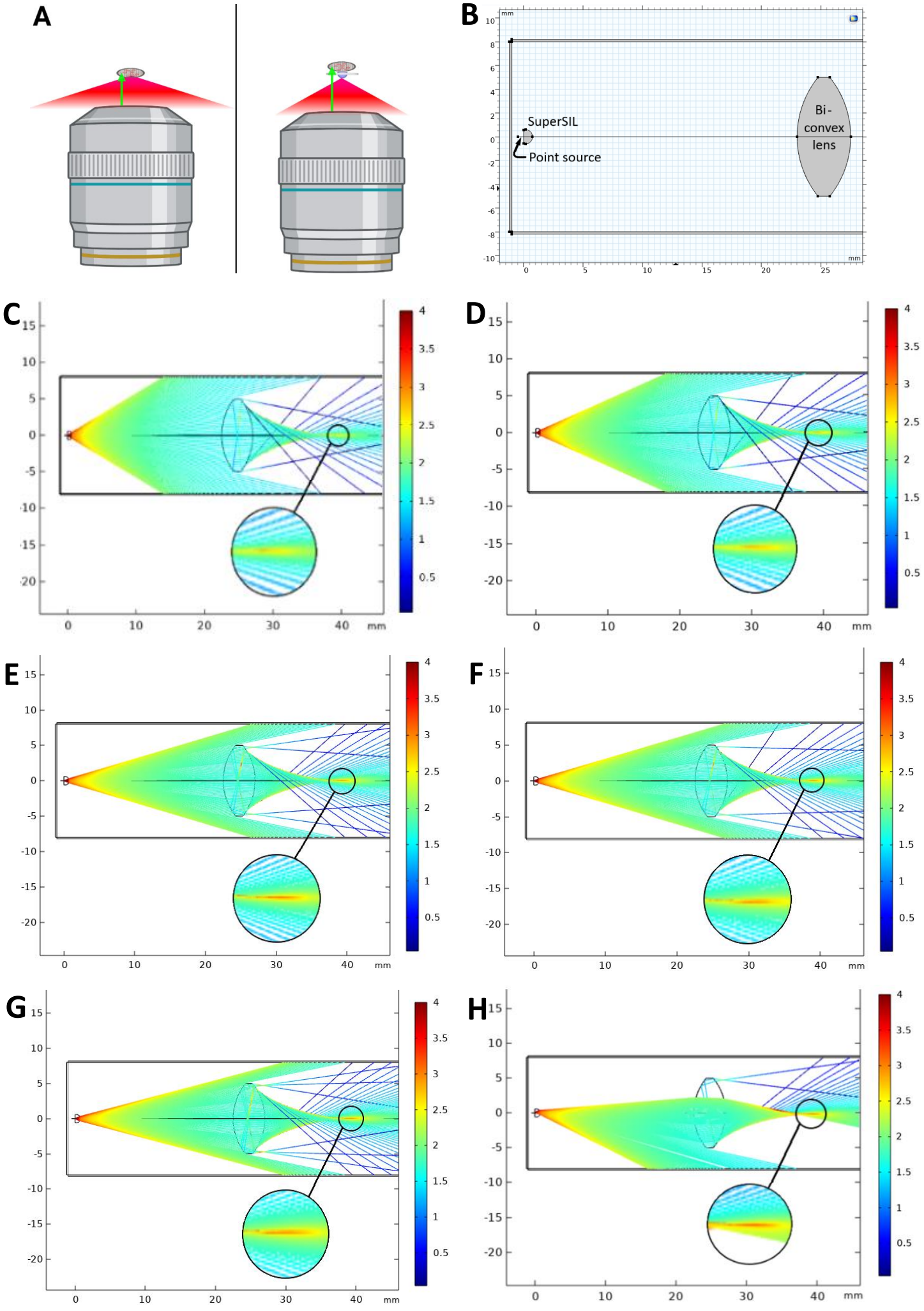
A
B
SuperSIL
Point source
Bi-convex lens
C
D
E
F
G
H
mm

instrument (Fig. 1A). The smallest beads were used only in this case, so they represent most accurately what the FLM does to a theoretical single point source. Other measurements demanded 0.5 µm beads (Fig. 1B-D), where values of 0.5 – 1.0 were measured in lateral dimensions and values varying between 1.0 – 3.0 µm were measured in the axial dimension. Now, we can check for improvements between different imaging conditions. As expected, the lateral resolution of our FLM is better than its axial resolution, because the PSF in the lateral directions are always <1.0 µm compared to always >1.0 µm in the axial direction. Furthermore, the overall resolution improved when the beads were imaged with SDCM (Fig. 1C+D) instead of widefield (Fig. 1B), as the lateral and axial values of SDCM never exceeded 0.7 µm and 2.0 µm respectively, whereas they did in widefield. However, when comparing SDCM results, the axial resolution under cryo-conditions (1.5 – 2.0 µm) (Fig. 1D) was slightly worse than at RT (1.0 – 1.5 µm) (Fig. 1C).

In addition to the lenses and contributions from all the components in the optical path, the measured PSF is also impacted by any drift. To estimate the contribution of drift to the determined PSFs, we directly measured the motion. Again, 0.5 µm beads were recorded in widefield mode both at RT and under cryo-conditions, and using all four available wavelengths. An image was taken every second, and the total recording time was 10 min per wavelength. The trajectories of numerous single beads were manually traced in ImageJ and their lengths were calculated. Shown are the typical start and end positions of one bead, and an arrow for the shifting direction (Fig. 1E). Most drift speeds at RT varied around 3 µm/h, whereas the speeds under cryogenic temperatures varied between 5-50 µm/h (Fig. 1F). These data quantitatively describe the baseline performance of our FLM, and can be used to show if the addition of the superSIL is beneficial.

Revisit superSIL design to predict ray trajectories with simulation tool COMSOL

To get a more quantitative insight into the optical behaviour of the superSIL within a FLM set-up, we wanted to simulate the ray trajectories that would be refracted by the lenses. In general, the effective NA of an objective lens can be enhanced by constructing lenses that capture more angles, or alternatively, by adding a higher RI material between the sample and the objective that re-directs photons towards the lens that would otherwise be lost. The superSIL's ability to improve the signal collection efficiency of the objective lens has the consequence of increasing the effective NA (Fig. 2A). The RI of the superSIL material is significantly higher than the RI of air, resulting in stronger convergence of the emitted light towards the objective lens. This is very convenient, especially at cryogenic temperatures when a long working distance is inevitable. To validate these assumptions, the Multiphysics program COMSOL® was used that can simulate physics of designs, devices and processes. A relatively simple 2D model was designed, which includes a point source that generated a cone of light, the superSIL, and a cylindrical biconvex lens (Fig. 2B). The geometry of the superSIL was taken from the Wang *et al.*, 2019 paper. Three parameters were tested to discover how they would affect the focal point after the biconvex lens in terms of centring rays and intensity.

First, we analysed ray propagation through various superSIL materials available from the superSIL manufacturer. These materials include cubic zirconia, sapphire and quartz with RIs of 2.17, 1.75 and 1.54 respectively (Fig. 2C-E). Ray convergence was reduced when cubic zirconia was replaced by sapphire, and quartz operated even less favourably, as shown by weaker intensities at the focal point. These results are in agreement with Equation (1), because the NA increases proportionally with the RI of the medium. So we decided to continue with a cubic zirconia lens during the rest of the simulations. The second variable investigated was the distance between the point source and the flat surface of the superSIL. This assesses the useful working distances and thereby provides an estimate for the maximum applicable sample thickness. The closest possible distance was 0.07 µm (Fig. 2E), since smaller values caused an error by the software. Other distances simulated were 0.1, 0.5, 1.0, 5.0 and 10.0 µm (Fig. 2F+G + Fig. S1). According to the simulation, the

Fig. 2 Simulations of superSIL optical behaviour. **A.** Illustration of an objective lens, sample on grid, and emission by the sample (red cone). In theory, the light cone of emitted signal without superSIL (left) should be narrowed with inclusion of superSIL (right). **B.** 2D model to simulate ray trajectories. Trajectories from SuperSIL materials quartz (**C**), sapphire (**D**), and cubic zirconia (**E**). The point source was located at 0.07 µm from the superSIL's flat surface in all cases unless otherwise stated. Distances of 1.0 µm (**F**) and 10.0 µm (**G**) shown here (additional distances shown in Fig. S1). **H.** The trajectories with the point source moved 100 µm upwards. In panels **C-H**, the focal point is enlarged to discern the subtle differences. Colours show values of light intensity (W / m^2) scaled logarithmically to observe changes in orders of magnitude.

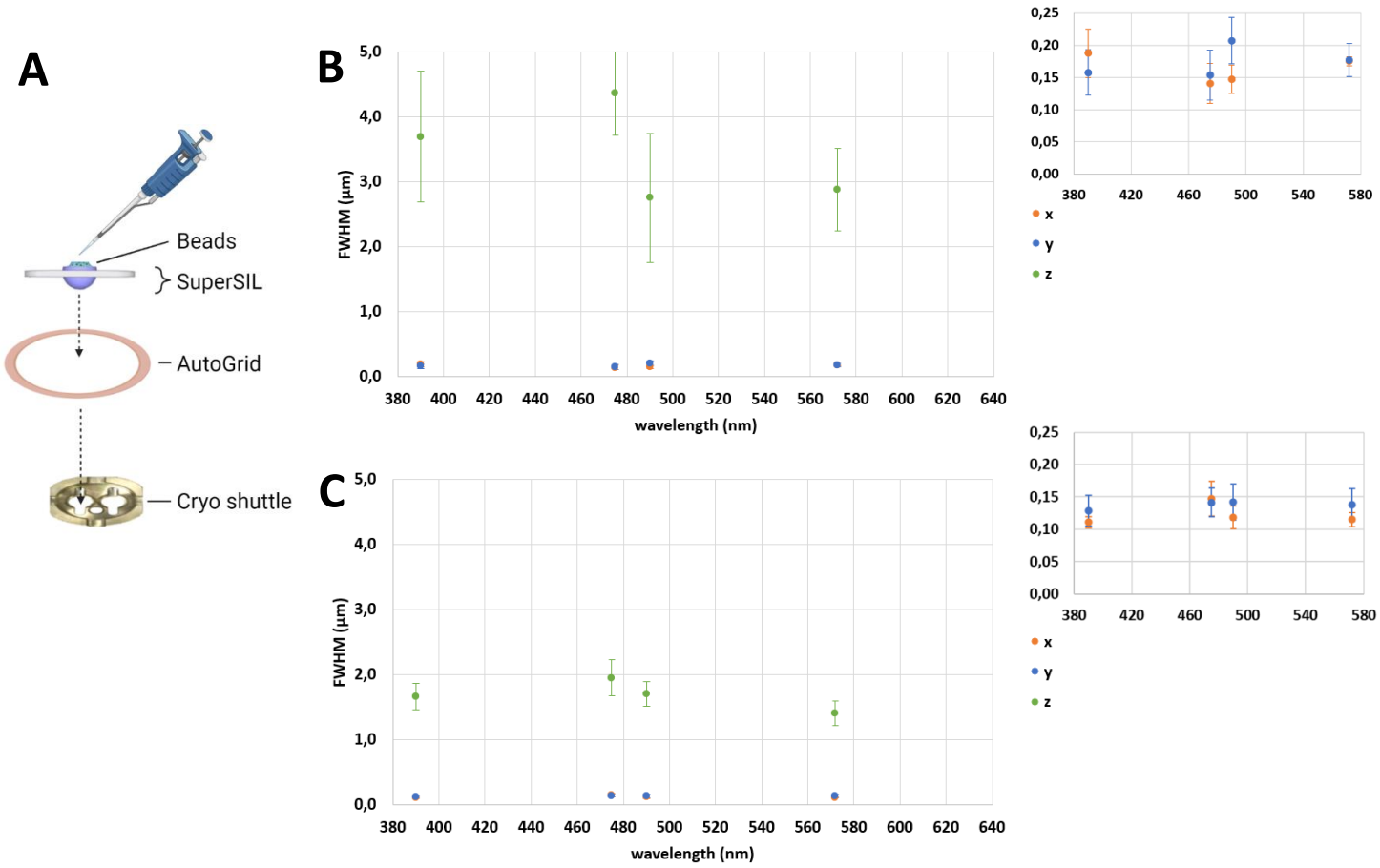

Fig. 3 Performance improved with the inclusion of the superSIL. **A.** Scheme for experimental setup where TetraSpeck beads were directly pipetted on the flat surface of the superSIL. **B+C.** PSF profiles in x (orange), y (blue) and z (green) directions. Here, 0.1 µm beads were imaged with widefield at RT (**B**) or under cryogenic conditions (**C**). The PSF plotting procedure was unchanged compared to Fig. 1. Error bars show the fluctuations across PSFs (n=8). The insets show the x and y dimensions at a different scale for clarity.

distinctions between 0.07, 0.1 and 0.5 µm were imperceptible, with the first subtle change remarked at 1.0 µm, where a larger, less intense smear around the focal point was observed. At 5.0 and 10.0 µm, the rays were deviated more prominently, resulting in diminished convergence and the focal point being less concentrated. Lastly, the space between point source and superSIL stayed 0.07 µm and the point source was moved 0.1 mm radially from the centre of the superSIL (Fig. 2H). The simulation showed that the rays focus at the same spot and were still centred as well as rays that emerged from a point source positioned in the absolute middle of the superSIL However, the main drawback is that the focal point was slightly more smeared out, which could increase the risk of axial blurring in the final image. Some main conclusions can be made after simulations with COMSOL. Firstly, as anticipated, when the RI of the superSIL's glass material is greater, the effective NA of the entire optical system will be higher as well. Secondly, the most ideal situation is reached when the sample is as close to the flat surface of the superSIL as possible. Consequently, the superSIL and objective lens couple can converge more rays, ultimately leading to a more accurate image. Thirdly, rays are consistently centred at the focal point sufficiently, even if the signal is emitted close to the edge of the superSIL.

Implementation of superSIL decreases the lateral PSF significantly

With this more comprehensive understanding of the superSIL, we decided to implement the original superSIL blueprint with as few modifications as possible (Wang *et al.*, 2019). Cubic zirconia was used for all superSIL devices where the lenses were placed in aluminium discs (Fig. S2). The next step was to include the superSIL in the current light microscope set-up. First, an already existing grid with calibration beads was placed against the flat surface of the superSIL. However, the cumbersome identification of the beads during imaging hindered trustworthy Z-stack acquisition. This is probably due to the unknown distance between the beads on the grid and the flat surface of the superSIL. As mentioned before, the closer the sample is to the superSIL, the better the focusing of the optical system. In addition, the field of view is very limited due to the high magnification the superSIL entails, which makes the search for isolated beads more complicated. On the other hand, 0.1 µm

beads were effortlessly imaged thanks to the additional magnifying ability of the superSIL, which was a welcome occurrence with regard to better PSF measurement accuracy. So instead of using grids, 0.1 µm beads were directly pipetted on the flat surface of the superSIL for maximal signal collection, and the superSIL itself fitted similarly in the set-up (Fig. 3A). The quantitative performance evaluation – both data collection and analysis – was repeated to make valid comparisons with previous obtained data. The only graph without involvement of the superSIL that can be used to compare the PSF profiles plotted here (Fig. 3B+C), is the graph that shows the widefield measurements at RT (Fig. 1A). Evident changes were observed in both axial and lateral directions. The lateral resolution improved from 0.4 – 0.5 µm without superSIL to around 0.11 – 0.25 µm with superSIL, coming outstandingly close to the true bead sizes (average delta = 0.05 µm). The axial resolution deteriorated, especially for the widefield at RT plus superSIL graph (Fig. 3B), where the axial values rose from mostly between 1.0 – 1.5 µm without superSIL to mostly >2.5 µm with supeSIL. Imaging under cryo-conditions (Fig. 3C) could restore the axial resolution back to about 1.5 – 2.0 µm. Hereafter, we also tried SDCM imaging, but no emission signal could be collected with 0.1, 0.5 or 1.0 µm beads. Thus, despite unresolved issues that must be addressed to present a convincing performance enhancement of our FLM, the introduction of the superSIL to the set-up yielded some positive results. Particularly the lateral resolution improved, and the axial resolution was comparable under cryogenic temperatures.

Widefield and SDCM images can be deconvolved with the determined PSF

Besides quantifying the performance of an instrument, the PSF can also be used to deconvolve images that are recorded with that same instrument. The observed signal and resolution from biological specimen usually include out-of-focus light that causes blurring in the final image, characterized by the PSF. Hence, by correcting the inherent optical limitations of an instrument computationally, the acquired data will benefit from an enhanced resolution. To do this, ImageJ was used for all processing steps. To obtain a reliable and accurate PSF, 20 clear single beads recorded with SDCM across different Z-stacks were isolated, centered, summed and masked. Then, the plugin DeconvolutionLab2 was used and required two inputs: an image to deconvolve and the PSF (Sage *et al.*, 2017). It also includes a variety of commonly used algorithms for different deconvolution purposes. Here, we deconvolved a SDCM image that was recorded with our FLM as well (Fig. 4A-D), by using the Richardson-Lucy with Total Variation (RLTV) algorithm (Dey *et al.*, 2006; Lucy, 1974; Richardson, 1972). Overall, as anticipated, the features in the image look cleaner and more refined after deconvolution, because it reduced the blurring of the high intensity fluorescent signals. Deconvolving the SDCM image made the zoomed out version seem brighter, but this effect is caused by the appearance of faint spots that vanished in the background before deconvolution. This observation was quantified by the line plots, which display an intensity increasement of the fluorescent signal while keeping the intensity of the background noise equal (Fig. 4E+F). To conclude, the resolution improves by deconvolving images with an established PSF. An intensity increasement of the fluorescent signal predominantly caused deblurring, effectively resulting in more details and the appearance of faint fluorescent spots.

Discussion

In this work, we show that the incorporation of the superSIL in our light microscope provided very promising results. Although the NA of our dry objective lens is only 0.9, the increased photon collection ability of the superSIL caused a major increase in effective NA and was confirmed with the simulations carried out in COMSOL Multiphysics and with observing an improvement in instrument performance characterized by the enhancement of the lateral resolution. Besides, the PSF acquired during performance evaluation was also used to successfully deconvolve a SDCM image.

However, measurements of the axial resolution yielded varying results, and were not consistent between RT and cryogenic conditions. Without the superSIL, the axial PSF was enlarged with SDCM under cryo-conditions when compared to RT, likely due to ice formation during the experiment, causing additional scattering. SDCM imaging avoids out-of-focus regions, and hence, less light hits the detector, making SDCM extra sensitive to the scattering effect. Contrastingly, the cryo-conditions diminished the size of the axial PSF for the widefield with superSIL measurements, thus improving the instrument performance. Considering these observations, we could assume that in this case little to no ice was present, but this would require further experiments to confirm. Thus, similar axial resolutions were initially expected when comparing room and cryogenic temperatures, but were not accomplished caused by the presence of ice. The addition of the superSIL also worsened the axial PSF, especially at RT. Probably, the insertion of another lens (and thus more glass) in the set-up could also lead to additional scattering. Interestingly, this occurrence was already predicted

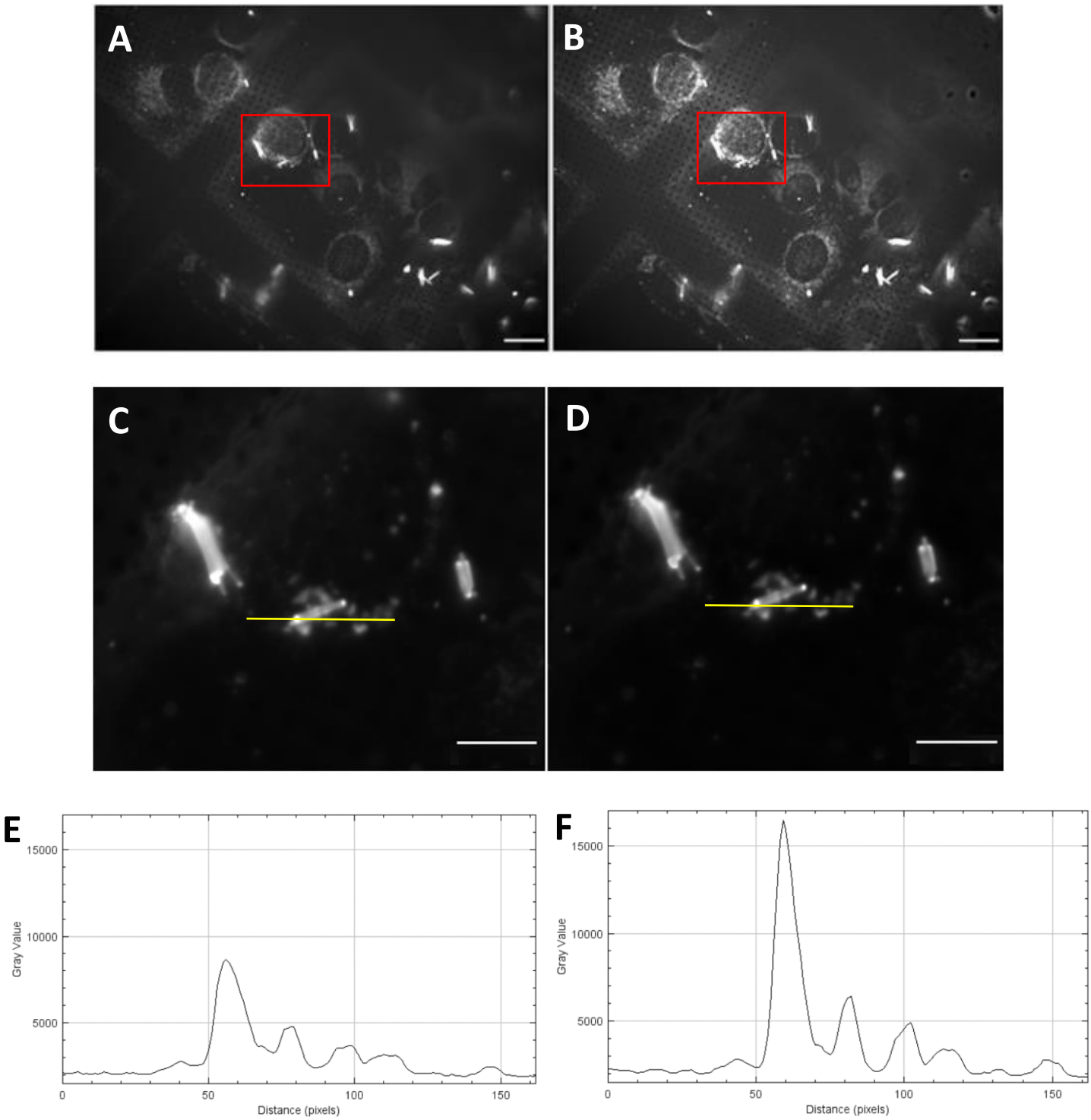

Fig. 4 PSF as tool to deconvolve a SDCM image with RLTV. Images were recorded with the same FLM as the PSF. The upper panels show the entire image before (**A**) and after (**B**) deconvolution, whereas the middle panels show the zoomed in image before (**C**) and after (**D**) deconvolution. The red squares in **A** and **B** indicate the region that was magnified in **C** and **D**. The yellow lines in **C** and **D** show the lines used to plot of the intensity in **E** and **F**. The brightness and contrast were not changed after deconvolution. Scale bars are 20 µm (**A+B**) and 10 µm (**C+D**).

during the COMSOL simulations, because the focal point was rather a spread over a larger area in axial direction than a symmetrical point. Unfortunately, time limitation did not allow us to discover the off-center limit of the superSIL where signal could still be detected. The only test tried was moving the point source 0.1 mm upwards (Fig. 2I). In general, COMSOL Multiphysics program proved that it could successfully simulate our proposed model, and with the required accuracy.

A significant limitation to the implementation of the superSIL was the imaging in SDCM mode. Emission signal by the calibration beads was never detected, not even when 0.5 or 1.0 µm beads were pipetted on the superSIL's flat surface instead of 0.1 µm beads. A plausible hypothesis would be that not enough light went through the spinning disk

component of our FLM, and this would apply for both illuminating and emitted light. Although extra photons are gathered by the superSIL, they could still be blocked by the spinning disk component. In addition, the signal that gets through the pinholes could be lost in the noise of the camera, so a lower noise floor on the camera would maybe help. Thus, the superSIL does not have to be the issue here, but this particular situation could be awkward. This is strengthened by the fact that the superSIL performed excellently with STORM, whereby a 2-fold resolution improvement was achieved (Wang *et al.*, 2019). They also hinted that superSILs could also be used for other super-resolution techniques, such as structured illumination microscopy (SIM) (Gustafsson, 2000), stimulated emission depletion microscopy (STED) (Hell & Wichmann, 1994) and photo activated localization microscopy (PALM) (Eric *et al.*, 2006). Undoubtedly, the practicality of superSIL implementation in a microscope set-up will differ between specific instruments, and definitely between imaging techniques, but this still needs to be determined.

The drift measurements to describe the motion of our instrument yielded inconsistent results. The drift speeds at RT were mostly around 3 µm/h, without any immense fluctuations. On the other hand, the drift speeds under cryo-conditions varied between 5-50 µm/h. The largest values were associated with blue illuminating light, and declined proportionally towards red illuminating light. It is important to mention that from blue to red light was also the order of measurements, whereas the order was random at RT. Besides, several measurements were carried out at RT, which was not the case under cryo-conditions. Because of recording under very cold circumstances, the illumination light could cause instrument heating, and temperature differences could promote increased motion. In addition, blue light has a shorter wavelength and thus more energy than red light, and therefore will heat the sample more. However, this inconsistent drift issue of our instrument was also noticed and reported. Apparently, the drift was abnormal shortly after starting up the instrument, and less drifting was perceived at a later stage. To find out the optimal conditions to record the drift with our FLM, we could investigate how long it would last before the sample temperature is stable after loading. The drift could also be effected by the liquid nitrogen level or flow around the objective lens, by the extra mass of the cryo-module and / or by additional scattering due to ice formation.

The acquired PSF was used to deconvolve a SDCM image. The PSF of an objective lens depends upon its NA, design, the contrast mode during image recording and the illuminating wavelength. The first three parameters are constant, leaving only the illuminating wavelength to possibly change the result after deconvolution. The separation of wavelengths could improve the deconvolution, because light with a shorter wavelength increases the resolution (see Equation 2). Hence, we could try to acquire a PSF with only blue light and to deconvolve the image with this.

The next planned steps were to use the superSIL in combination with cellular samples, and to perform cryo-CLM by using the FLM data to help guide the targeting for tomography data collection. For this purpose, yeast cells were grown where mitochondrial protein OM45 was fused to GFP. Then, the cells were pipetted on grids, and a “sandwich” was made of the grid containing the yeast cells plus the superSIL. To cool this sandwich down to cryogenic temperatures, a high pressure freezer (HPF) was used to make the grid stick to the flat surface of the superSIL. Unfortunately, the first attempt was unsuccessful due to the breaking of the superSIL. Hence, after reconsidering the sandwich design, a second attempt was carried out, but our HPF created a dangerous working environment in its new location. It remains uncertain how much the ROI targeting task will be helped by the addition of the superSIL.

In summary, superSILs can achieve high lateral resolution due to its ability of having a very high NA, resulting in increased photon collection. By including them in super-resolution microscopy set-ups, the resolution gap between cryo-FLM and cryo-EM will be lowered, making future cryo-CLEM experiments easier. Ultimately, it will have a major impact on the use of cryo-CLEM in cell and structural biology.

Materials & Methods

Fluorescent beads preparation

Tetraspeck beads (Invitrogen, Waltham, Massachusetts, USA) with sizes of 0.1, 0.5 and 1.0 µm were diluted with ultrapure water to make a range of concentrations (diluted by a factor of 10x, 100x or 1000x), sufficient to prevent the formation of large clumps of beads that would strongly interfere. Bead clump formation was further reduced by vortexing the tubes with the stock concentration and diluted beads before pipetting. Diluted beads were also sonicated for 5 min. Samples for widefield RT imaging without the superSIL were made by pipetting beads directly on cover slips, after cleaning the cover slips with 70% ethanol (v/v). For widefield and SDCM imaging under cryo-conditions without superSIL, samples were made by pipetting beads on clipped quantifoil R1/2 Cu 200 mesh grids. The latter method was also used for SDCM RT imaging. Beads were directly pipetted on the flat surface of the superSIL for imaging with the superSIL in the set-up. The metal disk that holds the lens fitted exactly in an AutoGrid, that successively fitted into the shuttle used in our FLM.

SuperSIL design

The 1 mm diameter superSILs (Knight Optical Ltd., UK) were made of uncoated cubic zirconia (ZrO2). This has a refractive index of 2.17, appropriate for superSIL microscopy (Wang et al., 2019). Lenses were mounted in 3 mm aluminium disks with a thickness of 0.2 mm and a central hole of 1.1 mm (diameter) (Fig. S2). The lenses were fixed with a temperature resistant adhesive (Masterbond) to ensure the flat surface of the lens stayed parallel to the plane of the aluminium disk.

PSF and drift measurements

The FEI CorrSight used contains two light sources for fluorescent imaging: a xenon bulb white light source (390, 475, 490, 572 nm excitation wavelengths created by filters) for widefield and a set of single wavelength lasers (405, 488, 561, 640 nm) for SDCM. A GFP emission filter was used when samples were excited with 475 nm and a DAPI/FITC/TexasRed emission filter was used for other wavelengths, whereas no emission filter was used for SDCM imaging. Objective lenses were cleaned if required. A Zeiss objective EC “Plan-Neofluar” 40x/0.9 Pol lens (Carl Zeiss, Oberkochen, Germany) was used for all PSF measurements. All components were calibrated and aligned properly before imaging.

Z-stacks were recorded for beads at both RT and under cryogenic conditions, and with or without the superSIL. The space between imaging planes in the axial direction was set to 0.1 µm for the smallest (0.1 µm) beads. These did not provide enough signal for the widefield cryogenic without superSIL data and for the SDCM data. Hence, 0.5 µm beads were used and spacing between planes was 0.25 µm.

Drift was measured by recording time lapses of 10 min, whereby one image per second was taken, and 990 ms between exposures. Measurements were carried out at both RT and under cryogenic temperatures, and beads were recorded in focus with the four earlier mentioned wavelengths of widefield mode. In this case, 0.5 µm beads were used to be certain that fluorescent signal could always be detected throughout each experiment.

Ray tracing simulations

The Ray Optics module within COMSOL Multiphysics was used as simulation program to study the intensity and behaviour of rays. The design of our model needed to reflect the reality, without making the model too sophisticated. A straightforward 2D model was created due to time and hardware constraints, which contained three main components. Firstly, a point source that generated a cone of light, whereby all rays would hit the superSIL. Secondly, the lens of superSIL (without the aluminium disk). Its geometry was taken from the Wang *et al.*, 2019 paper, and also matched our superSIL model (Fig. S2). Thirdly, a standard cylindrical biconvex lens made of Schott N-BK7 glass (RI = 1.515). The distance between the edge of the cylindrical biconvex lens and the spherical tip of the superSIL was 22.27 mm. The model performed in air at RT, and regular physical laws were simulated.

Data analysis – PSF profile of calibration beads

Z-stack data files were imported in ImageJ with Fiji as its distribution (Rueden *et al.*, 2017; Schindelin *et al.*, 2012). PSF sizes – expressed in terms of full width at half maximum height (FWHM) – of single beads were fitted and analysed with the MetroloJ plugin after cropping around them in xy dimensions (Matthews & Cordelières, 2010). These values were then averaged per wavelength (n=8) and graphically plotted.

Data analysis – Instrument drifting

Time lapse files were equivalently imported in ImageJ. The trajectory lengths of isolated beads (n=3) were manually inspected and determined per recorded time lapse. These values were then averaged per wavelength and graphically plotted as unconnected points, because gradual variation is absent.

Data analysis – Deconvolution with determined PSF

The same Z-stack data files used for determining PSF of instrument, were used here. Across different stacks, 20 isolated beads (5 per wavelength) were saved as separate files after cropping around them in xy dimensions. For each bead, the pixel with the highest intensity was identified with the FindFoci option of GDSC plugin (Herbert *et al.*, 2014), and then centered, so all pixels with the highest intensity had the same x,y,z position. Images were summed up to form one stack, and were converted from 16-bit to 32-bit. Next, to radially average the PSF over its full 360° area, the summed image was duplicated to obtain 16 copies. Axial symmetry was achieved by flipping 8 copies 180° in the axial direction. Next, each copy was rotated clockwise using this formula: (n-1) * 45° (Fig. S3). So the first and ninth copy were rotated 0°, the second and tenth copy 45°, the third and eleventh copy 90°, etc. These 16 images were summed again, and then multiplied by itself and masked, to ultimately get the end result (Movie 1). The widefield and SDCM image were deconvolved with the plugin DeconvolutionLab2 (Sage *et al.*, 2017), using the Richardson-Lucy with Total Variation algorithm, because it is adapted to Poisson noise that causes image degradation, and by integrating Total Variation, the edges in the image are preserved and homogeneous areas are smoothened (Dey *et al.*, 2006; Lucy, 1974; Richardson, 1972).

References

Asano, S., Engel, B. D., & Baumeister, W. (2016). In Situ Cryo-Electron Tomography: A Post-Reductionist Approach to Structural Biology. *Journal of Molecular Biology*, *428*(2, Part A), 332–343. DOI: 10.1016/j.jmb.2015.09.030

Betsig, E., Patterson., G. H., Sougrat, R., Lindwasser, O. W., Olenych, S., Bonifacino, J. S., Davidson, M. W., Lippincott-Schwartz, J., & Hess, H. F. (2006). Imaging Intracellular Fluorescent Proteins at Nanometer Resolution. *Science*, *313*(5793), 1642–1645. DOI: 10.1126/science.1127344

Cox, I. J., Sheppard, C. J. R., & Wilson, T. (1982). Improvement in resolution by nearly confocal microscopy. *Applied Optics*, *21*(5), 778–781. DOI: 10.1364/AO.21.000778

Dey, N., Blanc-Feraud, L., Zimmer, C., Roux, P., Kam, Z., Olivo-Marin, J.-C., & Zerubia, J. (2006). Richardson–Lucy algorithm with total variation regularization for 3D confocal microscope deconvolution. *Microscopy Research and Technique*, *69*(4), 260–266. DOI: 10.1002/jemt.20294

Elliott, A. D. (2020). Confocal Microscopy: Principles and Modern Practices. *Current Protocols in Cytometry*, *92*(1), e68–e68. DOI: 10.1002/cpcy.68

Faoro, R., Bassu, M., Mejia, Y. X., Stephan, T., Dudani, N., Boeker, C., Jakobs, S., & Burg, T. P. (2018). Aberration-corrected cryoimmersion light microscopy. *Proceedings of the National Academy of Sciences*, *115*(6), 1204 LP – 1209. DOI: 10.1073/pnas.1717282115

Gilkey, J. C., & Staehelin, L. A. (1986). Advances in ultrarapid freezing for the preservation of cellular ultrastructure. *Journal of Electron Microscopy Technique*, *3*(2), 177–210. DOI: 10.1002/jemt.1060030206

Gustafsson, M. G. (2000). Surpassing the lateral resolution limit by a factor of two using structured illumination microscopy. *Journal of Microscopy*, *198*(Pt 2), 82–87. DOI: 10.1046/j.1365-2818.2000.00710.x

Hell, S. W., & Wichmann, J. (1994). Breaking the diffraction resolution limit by stimulated emission: stimulated-emission-depletion fluorescence microscopy. *Optics Letters*, *19*(11), 780–782. DOI: 10.1364/ol.19.000780

Herbert, A. D., Carr, A. M., & Hoffmann, E. (2014). FindFoci: A Focus Detection Algorithm with Automated Parameter Training That Closely Matches Human Assignments, Reduces Human Inconsistencies and Increases Speed of Analysis. *PLOS ONE*, *9*(12), e114749. DOI: 10.1371/journal.pone.0114749

Kühlbrandt, W. (2014). The Resolution Revolution. *Science*, *343*, 1443–1444. DOI: 10.1126/science.1251652

Lucy, L. B. (1974). An iterative technique for the rectification of observed distributions. *The Astronomical Journal*, *79*, 745–754.

Marko, M., Hsieh, C., Schalek, R., Frank, J., & Mannella, C. (2007). Focused-ion-beam thinning of frozen-hydrated biological specimens for cryo-electron microscopy. *Nature Methods*, *4*(3), 215–217. DOI: 10.1038/nmeth1014

Matthews, C., & Cordelières, F. P. (2010). MetroloJ: an ImageJ plugin to help monitor microscopes' health. *Image J User & DeveloperConference*. Mondorf-les-Bains, Luxembourg.

Paddock, S. W., & Eliceiri, K. W. (2014). Laser Scanning Confocal Microscopy: History, Applications, and Related Optical Sectioning Techniques BT - *Confocal Microscopy: Methods and Protocols* (S. W. Paddock (ed.); pp. 9–47). Springer. DOI: 10.1007/978-1-60761-847-8_2

Richardson, W. H. (1972). Bayesian-Based Iterative Method of Image Restoration*. *Journal of the Optical Society of America*, *62*(1), 55–59. DOI: 10.1364/JOSA.62.000055

Rigort, A., Bäuerlein, F. J. B., Villa, E., Eibauer, M., Laugks, T., Baumeister, W., & Plitzko, J. M. (2012). Focused ion beam micromachining of eukaryotic cells for cryoelectron tomography. *Proceedings of the National Academy of Sciences*, *109*(12), 4449 LP – 4454. DOI: 10.1073/pnas.1201333109

Rueden, C. T., Schindelin, J., Hiner, M. C., DeZonia, B. E., Walter, A. E., Arena, E. T., & Eliceiri, K. W. (2017). ImageJ2: ImageJ for the next generation of scientific image data. *BMC Bioinformatics*, *18*(1), 529. DOI: 10.1186/s12859-017-1934-z

Rust, M. J., Bates, M., & Zhuang, X. (2006). Sub-diffraction-limit imaging by stochastic optical reconstruction microscopy (STORM). *Nature Methods*, *3*(10), 793–796. DOI: 10.1038/nmeth929

Sage, D., Donati, L., Soulez, F., Fortun, D., Schmit, G., Seitz, A., Guiet, R., Vonesch, C., & Unser, M. (2017). DeconvolutionLab2: An open-source software for deconvolution microscopy. *Methods*, *115*, 28–41. DOI: 10.1016/j.ymeth.2016.12.015

Sartori, A., Gatz, R., Beck, F., Rigort, A., Baumeister, W., & Plitzko, J. M. (2007). Correlative microscopy: Bridging the gap between fluorescence light microscopy and cryo-electron tomography. *Journal of Structural Biology*, *160*(2), 135–145. DOI: 10.1016/j.jsb.2007.07.011

Schellenberger, P., Kaufmann, R., Siebert, C. A., Hagen, C., Wodrich, H., & Grünewald, K. (2014). High-precision correlative fluorescence and electron cryo microscopy using two independent alignment markers. *Ultramicroscopy*, *143*, 41–51. DOI: 10.1016/j.ultramic.2013.10.011

Schindelin, J., Arganda-Carreras, I., Frise, E., Kaynig, V., Longair, M., Pietzsch, T., Preibisch, S., Rueden, C., Saalfeld, S., Schmid, B., Tinevez, J.-Y., White, D. J., Hartenstein, V., Eliceiri, K., Tomancak, P., & Cardona, A. (2012). Fiji: an open-source platform for biological-image analysis. *Nature Methods*, *9*(7), 676–682. DOI: 10.1038/nmeth.2019

Schur, F. K. M. (2019). Toward high-resolution in situ structural biology with cryo-electron tomography and subtomogram averaging. *Current Opinion in Structural Biology*, *58*, 1–9. DOI: 10.1016/j.sbi.2019.03.018

Wang, L., Bateman, B., Zanetti-Domingues, L. C., Moores, A. N., Astbury, S., Spindloe, C., Darrow, M. C., Romano, M., Needham, S. R., Beis, K., Rolfe, D. J., Clarke, D. T., & Martin-Fernandez, M. L. (2019). Solid immersion microscopy images cells under cryogenic conditions with 12 nm resolution. *Communications Biology*, *2*(1), 1–11. DOI: 10.1038/s42003-019-0317-6

Supplementary Figures

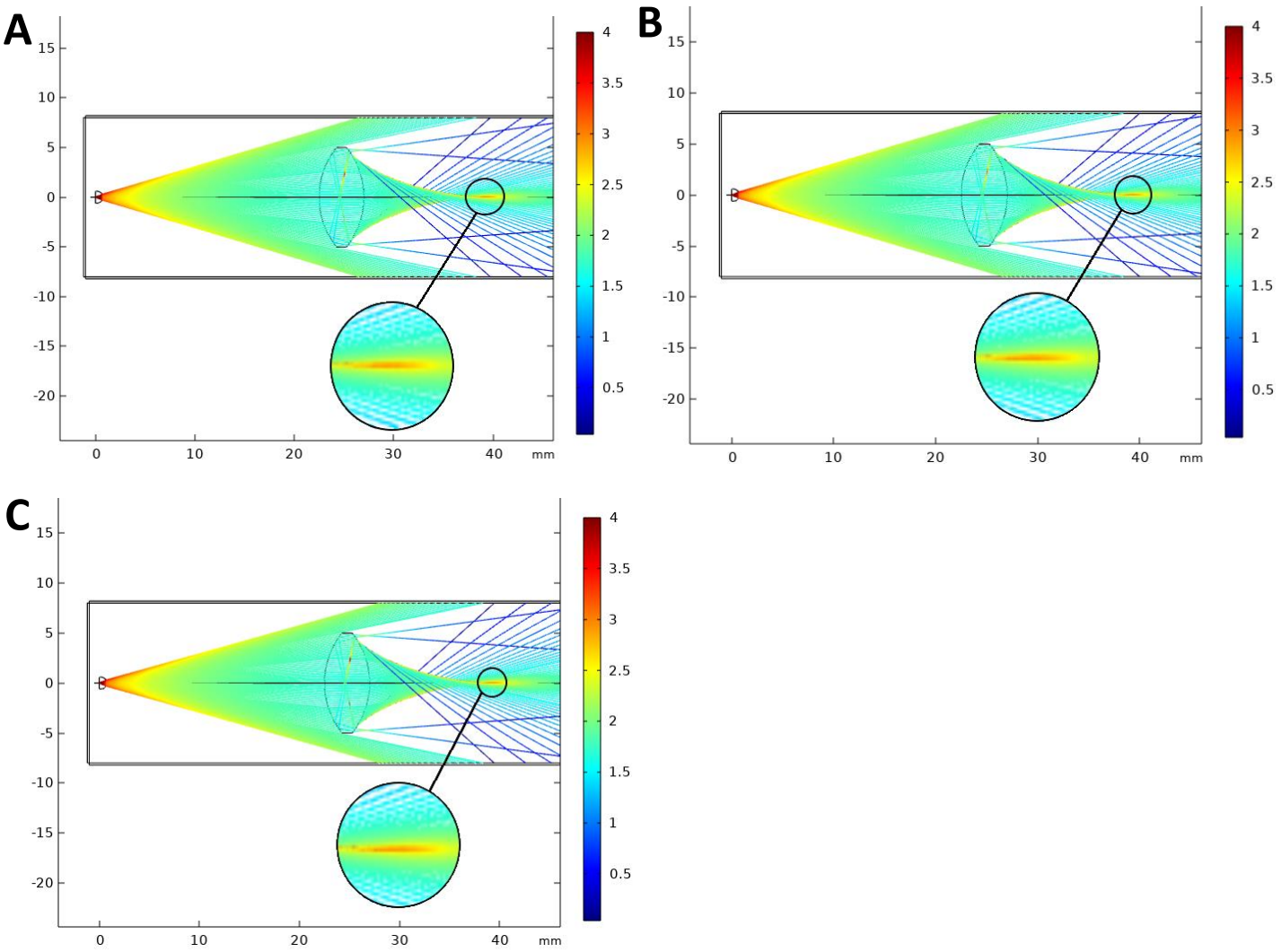

Fig. S1 Simulations of different distances between the point source and the flat surface of the superSIL. Distances 0.1 µm (**A**), 0.5 µm (**B**) and 5.0 µm (**C**) are shown. The focal point is enlarged to discern the subtle differences. Colours show values of light intensity (W / m^2) scaled logarithmically to observe changes in orders of magnitude.

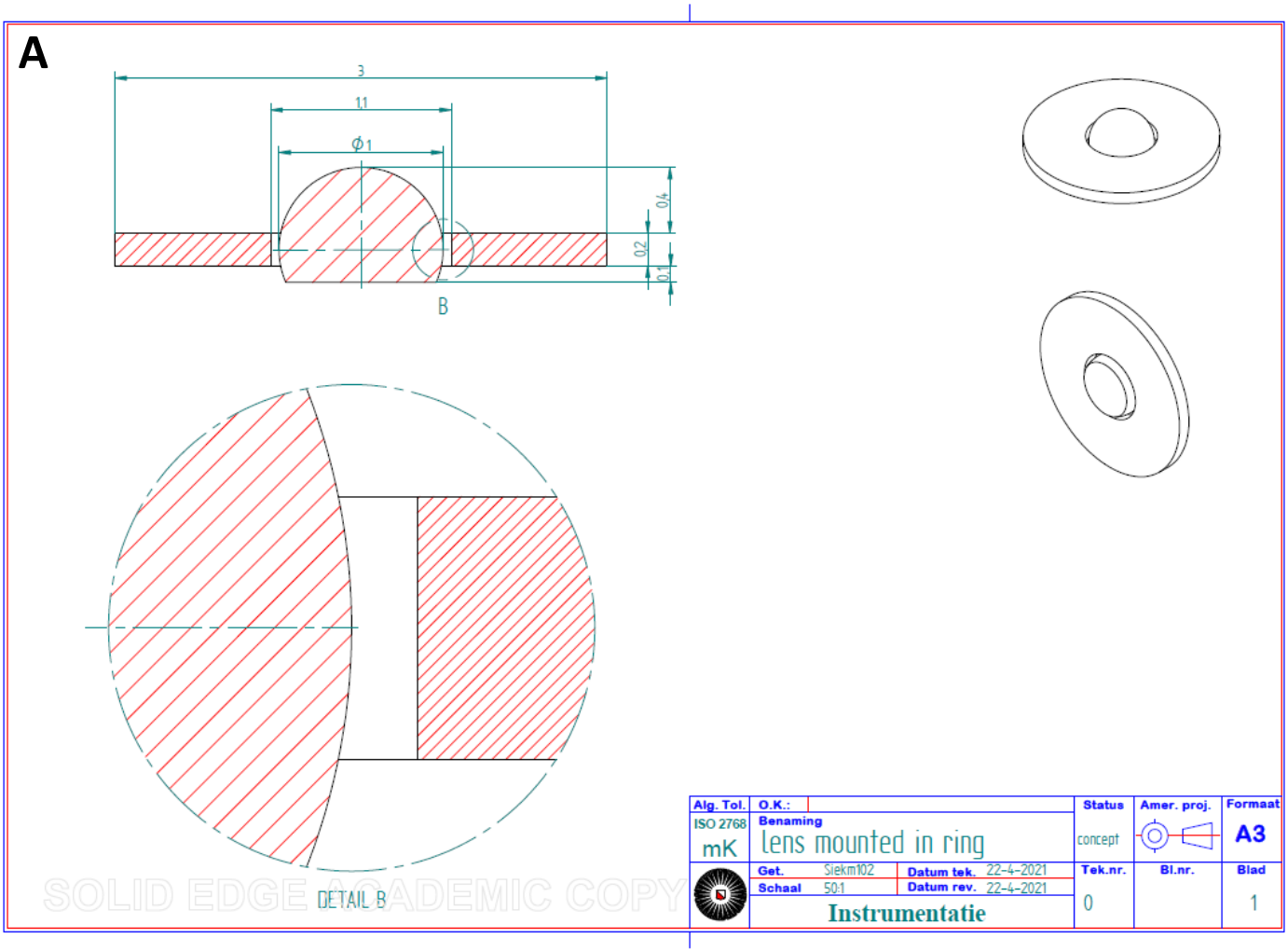

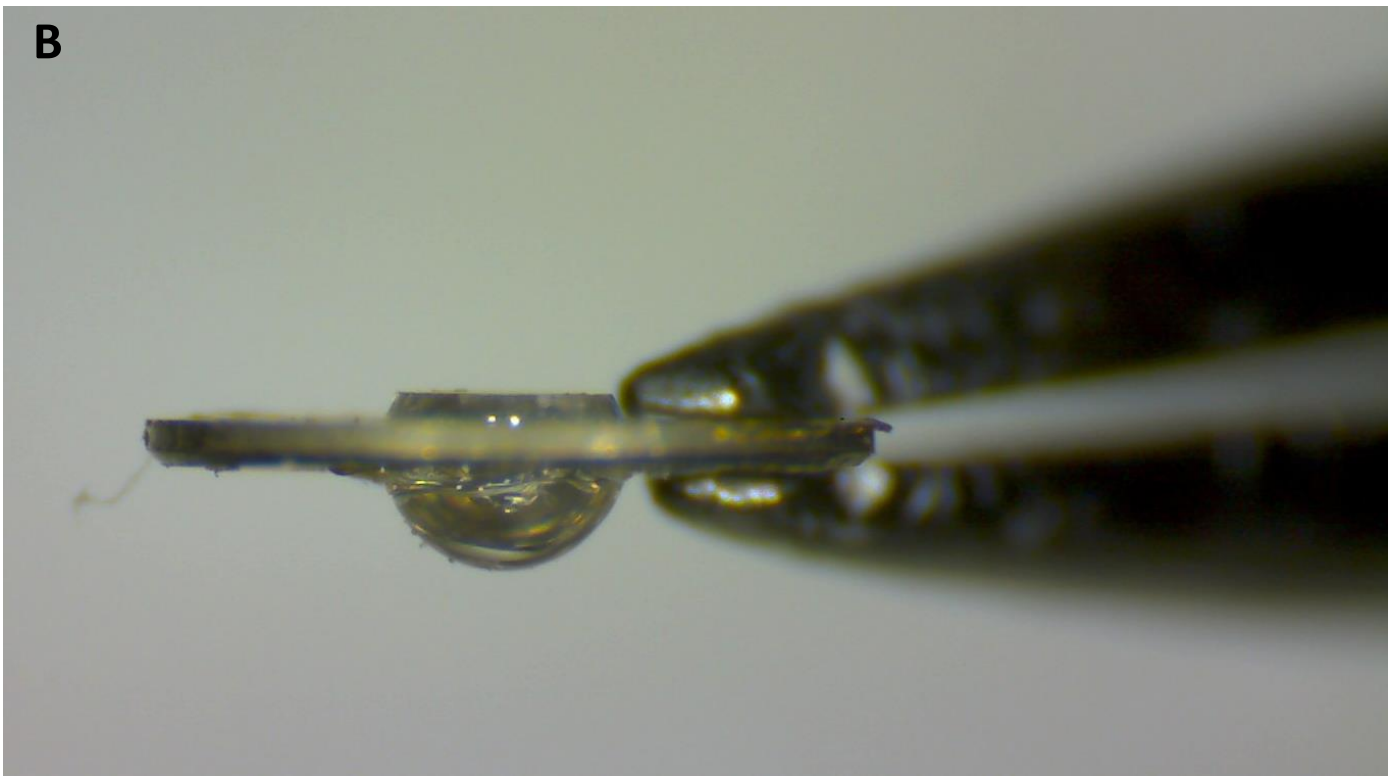

Fig. S2 The design and assembly of the superSIL. A. The technical drawing of the superSIL in its aluminium disk. Values are in mm. Detail B demonstrates the space between the lens and the disk where the adhesive was applied. The images in the right upper corner show both the flat side and the spherical side of the superSIL. **B.** Photo of the superSIL shortly after it was mounted in its disk.

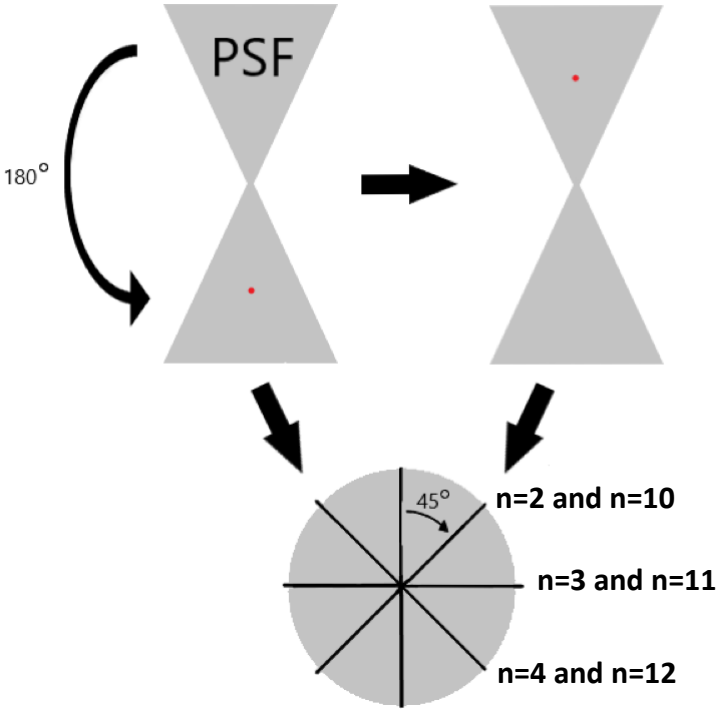

Fig. S3 Radial averaging process for an evenly spread PSF. The full 360° area was covered uniformly by duplication of the PSF after image summing. 8 copies were flipped in the axial direction, and all 16 copies were clockwise using this formula: (n-1) * 45°. These 16 resulted images were summed again afterwards.